Droplet bouncing and jump-off forces on ridged substrates

Juan Li,[1,2] Baixue Li,[1,2] Alexander Oron,[2] and Youhua Jiang[1,2,*]
[1]*Department of Mechanical Engineering, Guangdong Technion–Israel Institute of Technology, Shantou, Guangdong 515063, China*
[2]*Faculty of Mechanical Engineering, Technion–Israel Institute of Technology, Haifa 3200003, Israel*

(Received 10 May 2024; accepted 29 August 2025; published 25 September 2025)

It seems to be common sense that decreasing the pore size of a mesh surface, thereby enhancing the capillary pressure resisting the liquid penetration, is the only way to suppress its penetration. Here, we demonstrate that a macro-ridge created on a mesh surface increases its dynamic pressure threshold for liquid penetration by a droplet by up to 130%. This phenomenon is attributed to the symmetry and synchronicity breaking of the flow-focusing process during the retraction stage of droplets. Based on multiple flow-focusing events of separate liquid films at different sites that take place synchronically and independently, experiments and analyses are conducted to capture the timescale, magnitude, and the resultant pressure of the droplet jump-off force imparted onto ridged substrates, despite the variations in droplet impact speed, liquid viscosity, and the ridge morphology.

DOI: 10.1103/cz2d-3vsd

I. INTRODUCTION

It seems to be common sense that the only way of improving the resistance of a mesh surface representing a simplified model of a face mask [1–3] to an impacting droplet which imparts the dynamic pressure of $\sim\rho V_0^2/2$ is to enhance the capillary pressure $4\gamma_{LV}/w$ by decreasing the mesh pore width w [4–6], where ρ, V_0, and γ_{LV} represent the liquid density, droplet impact speed, and liquid-vapor interfacial tension, respectively. This concept of pressure balance is also critical to the stability of surface superhydrophobicity (the wetting state with low droplet adhesion) [7], where the substrate is partially wetted with the liquid-vapor interface suspended between micro-/nanostructures referred to as the Cassie-Baxter state [8]. The Cassie-Baxter state may transit to the undesired Wenzel state (the wetting state with high droplet adhesion) [9], i.e., the surface voids are fully wetted, when the pressure imposed by a droplet overcomes the capillary pressure provided by the surface structures [10–12]. Except for complex surface micro-/nanostructures, the enhancement of superhydrophobicity stability is intuitively enabled by decreasing the size of voids in between the solid structures [10,13]. However, a decrease in the size of voids causes an increase in the surface solid fraction, i.e., the ratio of actual solid-liquid contact area to the projected area of a droplet onto the substrate, which adversely results in an increase in droplet adhesion [14–16]. This leads to the core question of this study: Is it possible to suppress droplet penetration through/into surface pores/voids while not compromising the surface functionality (e.g., low droplet adhesion and breathability of a mask [17,18])?

Prior studies showed that an impacting droplet imposes two forces onto a superhydrophobic substrate. The inertia-governed first force (the impact force) $\sim\rho V_0^2 D_0^2$, where D_0 is the droplet diameter before touching the substrate, occurs in the spreading phase [19–21]. Depending on the

[*]Contact author: youhua.jiang@gtiit.edu.cn; youhua.jiang@technion.ac.il

value of the Weber number ($\mathrm{We} = \rho D_0 V_0^2/\gamma_{LV}$), the mechanism of the emergence of the second force varies [20]. Specifically, for small We (<30), the second force is associated with a singular jet caused by the collapse of an air cavity. For $30 < \mathrm{We} < 100$, the second force (the jump-off force F_j) originates from the horizontal-to-vertical redirection of the momentum of the retracting droplet (a process known as the flow focusing) over an effective area A_{eff} and over a time interval termed flow-focusing time [6,22–24]. For large We (>100) of water droplets, the second force is fluctuating and vanishing because the droplet retraction and the following flow focusing are hindered by the droplet rim instability and splashing [23].

Prior studies showed that the second force generates a larger pressure P_j than that of the first force because A_{eff} is smaller than the droplet base $\sim D_0^2$. As such, the threshold droplet dynamic pressure causing liquid penetration through a mesh is determined by the jump-off force F_j and pressure P_j rather than the impact force $\sim \rho V_0^2 D_0^2$ or pressure $\sim \rho V_0^2$ [6]. With respect to surface superhydrophobicity, previous studies have similarly demonstrated that the Cassie-to-Wenzel wetting transition predominantly occurs during the retraction phase of the droplet evolution, rather than during its initial impact or spreading stages [25]. This suggests that for studies concerning the penetration of a mesh or the breakdown of superhydrophobicity [9–12], the droplet jump-off force F_j and the jump-off pressure P_j are of primary interest, which constitute the central focus of the present investigation. Accordingly, the ability to manipulate the jump-off force and pressure through surface design emerges as a critical aspect in controlling droplet-surface interactions. Macro-ridges placed on a substrate alter droplet jump-off dynamics by breaking the symmetry of droplet retraction, causing droplet splitting and a reduction in the droplet-substrate contact time [26–28]. As inspired, a droplet released at a height H of 44 mm was allowed to impact onto a flat [Fig. 1(a)] and ridged [Fig. 1(b)] superhydrophobic mesh, both of which were textured with square pores with a width w of 0.1 mm and edge-to-edge spacing s of 0.05 mm [Fig. 1(e)]. Figure 1(a) illustrates the prior observation that only the second penetration caused by the jump-off force (second force) takes place, whereas the impact force (first force) failed to cause penetration [6]. Therefore, the dynamic pressure threshold $\rho V_0^2/2$ leading to the mesh penetration is determined by the second penetration when the droplet recedes. In comparison, Fig. 1(b) shows that the same droplet released at the same height fails to penetrate the mesh when a ridge with the cross-section of a triangle (0.3 mm in size) is placed between two arrays of pores ["I"-shape ridge, see the inset of Figs. 1(d) and 1(e)], where the spacing between the pore and the ridge is 0.05 mm. We thus conjecture that the presence of a ridge reduces the second force and pressure imparted to the mesh.

We find that this macro-ridged mesh requires a threshold value of the droplet release height H of 105 mm for liquid penetration by the second force (Fig. 1(c), see also Video S1 in the Supplemental Material [29]). At this release height, both the first penetration caused by the impact force and the second penetration caused by the jump-off force are observed. Specifically, while the first penetration proceeds, the main droplet splits into two droplets as the liquid along the ridge (into the paper plane) recedes much faster than the rest [27]. Each splinter droplet keeps receding, independently causing the second liquid penetration. The threshold dynamic pressure values $\rho V_0^2/2$ causing the first and second penetrations on flat and "I"-shape ridged meshes are presented *versus* the capillary pressure $4\gamma_{LV}/w$ resisting liquid penetration in Fig. 1(d), where the pore edge spacing s is fixed and the pore width w ranges from 0.08 mm to 0.25 mm. The threshold value $\rho V_0^2/2$ for the first penetration is not affected by the presence of the ridge because the latter (with the size of ~0.3 mm) cannot affect the inertia-dominated impact dynamics of the droplet with the diameter D_0 of 2.3 mm. In comparison, a 130% increase in the threshold value $\rho V_0^2/2$ for the second penetration due to the presence of the ridge suggests counterintuitive evidence that the droplet jump-off force/pressure can be mitigated to suppress liquid penetration without decreasing the pore size.

Based on the above evidence, we aim to investigate how the ridge morphology determines the jump-off force/pressure. To avoid the complex jump-off forces caused by air cavity collapse (singular jet) at low We [20,30,31] and the fluctuating and vanishing jump-off forces caused by

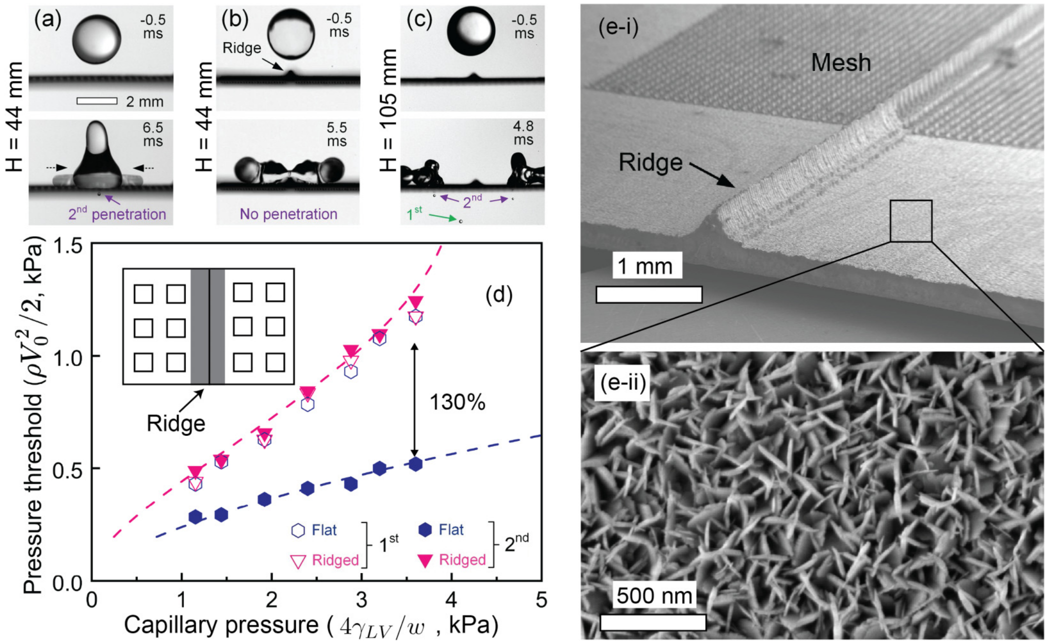

FIG. 1. Impact dynamics of a droplet released at 44 mm onto (a) a flat and (b) an "I"-shape ridged mesh, showing liquid penetration in retraction and no penetration, respectively. (c) Impact dynamics of a droplet released at 105 mm onto a ridged mesh, where liquid penetration takes place in both spreading (first penetration) and retraction (second penetration) stages. (d) The threshold droplet dynamic pressure (dots) is shown *versus* the capillary pressure for both the first and second penetrations, where the dashed lines follow Eq. (9) with a prefactor of 0.38. Inset: the sketch of the mesh geometry. (e) Scanning electron microscopy image of the ridged superhydrophobic mesh.

droplet splashing at high We [32–34], we intentionally narrow our primary experimental data range to $25 < \mathrm{We} < 170$ [35–38] while varying the liquid viscosity μ (Reynolds number $60 < \mathrm{Re} = \rho D_0 V_0/\mu < 3800$) and substrate ridge morphology. Together with the visualized droplet dynamics, we examine the timescale, magnitude, and resulting pressure of the droplet jump-off force imparted onto these substrates. We also provide explanations for the variation ranges of the parameters used in the experiments.

II. EXPERIMENTS AND METHODS

In addition to a flat superhydrophobic substrate, we prepare three ridge configurations referred to as the "I"-shape ridge, the "Y"-shape ridge, and the "+"-shape ridge, corresponding to an equal division of the substrate into two, three, and four equal domains, respectively. Ridged substrates (without pores) were prepared by selectively removing the surface material of an aluminum plate (1 mm in thickness) using a laser etcher (HS50II, Han's Group, China). Flat meshes were prepared by drilling square pores from an aluminum plate (0.2 mm in thickness), and the ridged meshes were prepared by drilling pores from the ridged substrate with the spacing between the ridge and pore of 0.05 mm [see SEM images in Fig. 1(e)]. All aluminum substrates were superhydrophobilized using a process known as boehmitization, followed by chemical vapor deposition of 1H,1H,2H,2H-Perfluorodecyltrichlorosilane [23], exhibiting DI water droplet advancing and receding contact angles of $160° \pm 5°$ and $155° \pm 5°$, respectively. The impact force was recorded by a piezoelectric sensor (9215A, KISTLER, Switzerland) placed beneath the substrate at a sampling

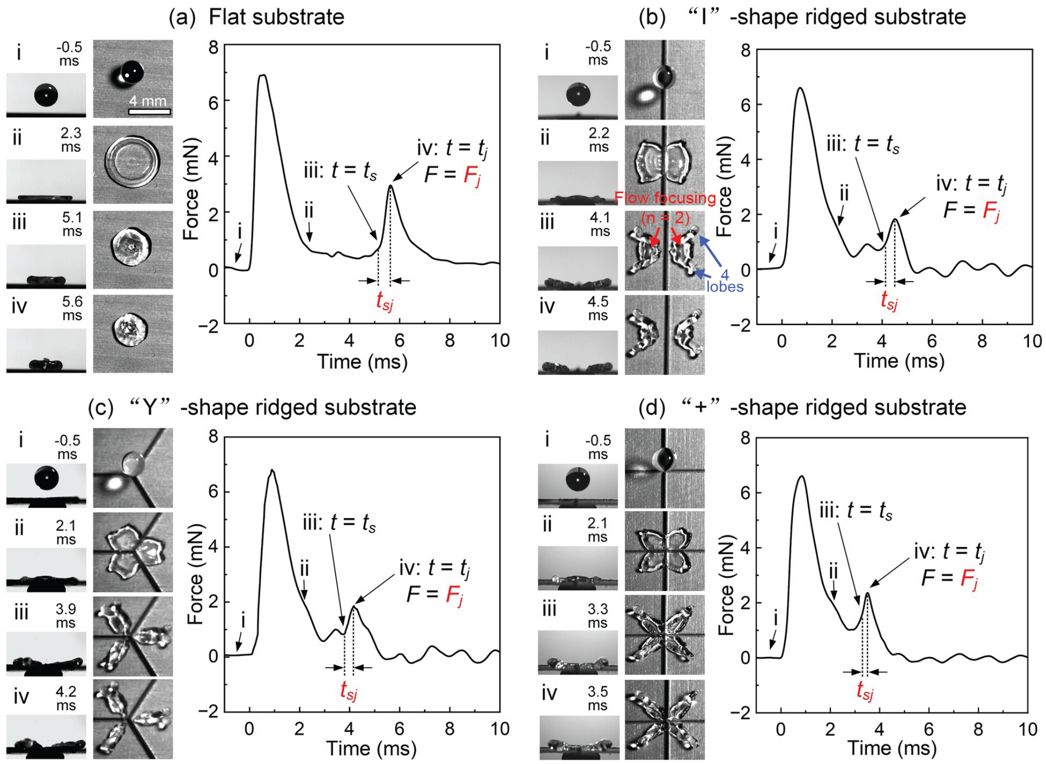

FIG. 2. Temporal variation of the force exerted onto a (a) flat, (b) "I"-shape ridged, (c) "Y"-shape ridged, and (d) "+"-shape ridged superhydrophobic substrate by a droplet released at 80 mm. The images represent droplet morphology at (i) 0.5 ms before the impact, (ii) the moment right before the liquid retreats along the ridge, (iii) the moment when the jump-off force starts to increase abruptly at t_s, and (iv) the moment when the jump-off force reaches its peak F_j at t_j.

rate of 2×10^5 Hz. The side and top views of the droplet dynamics were captured using two synchronized high-speed cameras at 10 000 fps (Nova S16, Photron, Japan).

Deionized (DI) water droplets ($\rho = 998\ \mathrm{kg/m^3}$, $\gamma_{LV} = 0.072$ N/m, $\mu = 1.0$ mPa s) of diameters $D_0 = 2.3 \pm 0.1$ mm and $D_0 = 2.7 \pm 0.1$ mm were released at heights varying from 40 mm to 100 mm, corresponding to $25 < \mathrm{We} < 73$ and $2000 < \mathrm{Re} < 3800$. To examine the effects of viscosity, droplets of $D_0 = 2.3 \pm 0.1$ mm made with water-glycerol mixtures (45, 60, and 75 wt% of glycerol) were allowed to impact onto the flat superhydrophobic substrate from heights varying from 40 mm to 220 mm, corresponding to $30 < \mathrm{We} < 170$ and $60 < \mathrm{Re} < 1100$. The viscosity of water containing 45 wt%, 60 wt%, and 75 wt% of glycerol is 4.5 mPa s, 10.0 mPa s, and 36.7 mPa s, respectively, while their γ_{LV} remains almost constant with the minimal value of 0.067 N/m. The increase in the maximal release height of viscous droplets results from the increase in the range of measurable jump-off forces because the viscous effects suppress the droplet splashing. To examine the synergistic effects of ridge morphology and liquid viscosity, 75 wt%-glycerol droplets ($D_0 = 2.3 \pm 0.1$ mm) were allowed to impact onto all ridged substrates with release heights varying from 40 mm to 120 mm. The upper bound of the release height for ridged substrates compared to that for a flat substrate was reduced because the ridge presence promotes droplet splashing. The reported experimental data are taken as the average of at least five reproducible experiments. The sets of experimental parameters used here are also presented in the legend of Fig. 3(a) for better readability.

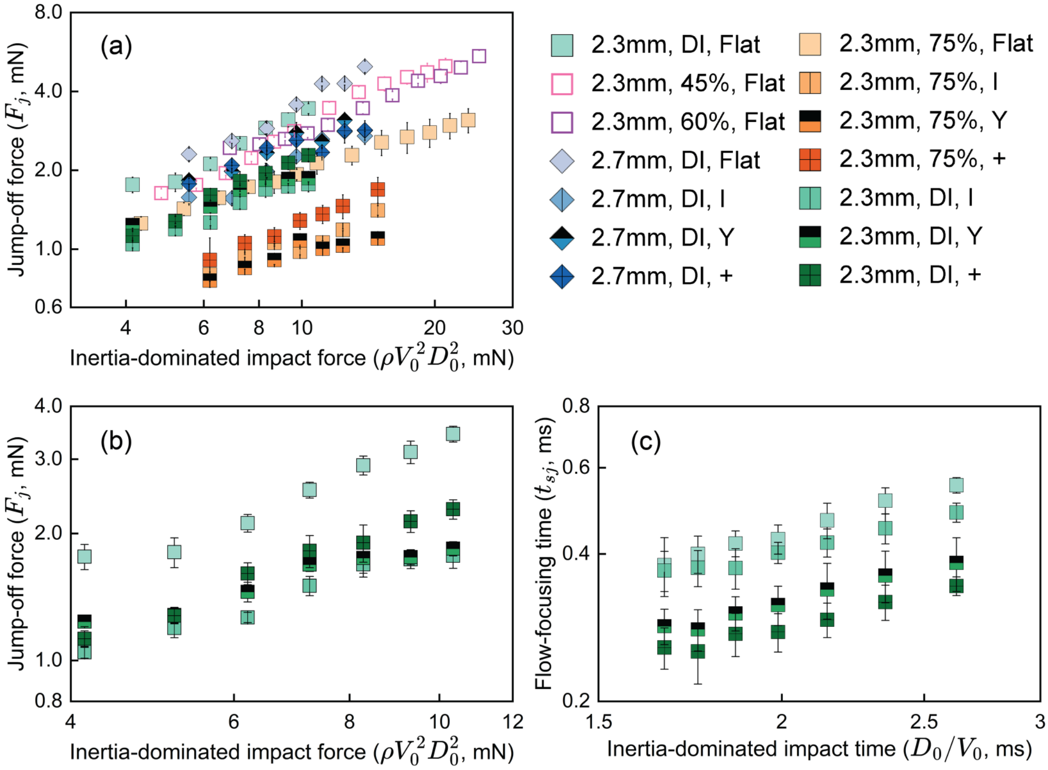

FIG. 3. (a) Variation of the measured droplet jump-off force F_j *versus* the inertia-dominated impact force $\rho V_0^2 D_0^2$ for droplets with different properties and on substrates with different ridge shapes. The legend is in the order of droplet diameter, Glycerol weight percentage (DI for pure water), and ridge morphology. (b) Replot of the jump-off force F_j for water droplets ($D_0 = 2.3$ mm) on substrates with varying morphologies. (c) Variation of the measured flow-focusing time t_{sj} *versus* the inertia-dominated impact time D_0/V_0 for water droplets.

III. RESULTS AND DISCUSSION

A. Measured force profiles and the corresponding droplet dynamics

Using water droplets of $D_0 = 2.3$ mm released at 80 mm as an example, temporal variations are presented for the force exerted onto the flat [Fig. 2(a)], "I"-shape ridged [Fig. 2(b)], "Y"-shape ridged [Fig. 2(c)], and "+"-shape ridged [Fig. 2(d)] substrates, where the first and the second force peaks are associated with the droplet impact and the droplet jump-off, respectively (see also Video S2). We label the main events of the droplet-substrate interaction based on the measured forces, including (i) 0.5 ms before the droplet-substrate contact, (ii) the onset of liquid retraction (liquid retraction along the ridge for ridged substrates), (iii) the emergence of F_j due to the droplet squeezing (signified by a sudden change in the slope of force profiles), $t = t_s$, and (iv)F_j reaching its peak, $t = t_j$.

As compared to the case on flat substrates [Fig. 2(a)], F_j on ridged substrates takes place much earlier [Figs. 2(b)–2(d)]. This agrees with the reduced droplet-substrate contact time on ridged substrates, and both phenomena result from the faster liquid retraction along the ridge than that on the flat areas [27,28]. At the maximum spreading (stage ii), the main droplet is equally divided into two ($n = 2$), three ($n = 3$), and four ($n = 4$) films by the "I"-, "Y"-, and "+"-shape ridges, respectively. Those films then reconfigure in a complex manner; for example, in agreement with Gauthier *et al.* [28], where the films on the "I"-shape ridged substrate reconfigure to a butterfly shape with four lobes at four corners [Figs. 2(b-iii) and 2(b-iv)], which may suggest $n = 4$ instead of $n = 2$ as a characteristic number representing the effects of ridges in the following analysis. Nevertheless, we find that the four lobes at the corners do not contribute to the droplet jump-off force F_j (the matter of interest), because F_j originates from the squeezing of receding liquids (flow focusing). Instead, the four lobes keep spreading without squeezing being previously reported to be closely correlated with the contact time [28], which is one order of magnitude larger than the flow-focusing time (see Video S2). In comparison, as marked in Fig. 2(b-iii), the liquid film recoiling from the ridge and in the direction perpendicular to the ridge collides (its occurrence coincides with the emergence of F_j), causing the flow to focus on each side of the ridge (hence, $n = 2$). Following the same logic, for the "Y"-shape ridged substrate, three flow-focusing events take place synchronically when the liquid films recoil from the adjacent ridges, suggesting $n = 3$. Similarly, for the "+"-shape ridged substrate, four flow-focusing events, each located within the area between the adjacent ridges (a quadrant), suggest $n = 4$. To sum up, the number $n = 1$, 2, 3, and 4 of flow-focusing events take place on flat [Fig. 2(a)], "I"-shape ridged [Fig. 2(b)], "Y"-shape ridged [Fig. 2(c)], and "+"-shape ridged [Fig. 2(d)] substrates, respectively. In the following text, n, being both the number of equally divided films by the ridges and the number of flow-focusing events, serves as the characteristic number representing the effects introduced by the ridges.

B. Experimental values of the jump-off force and the flow-focusing time

All measured jump-off forces F_j are plotted versus the inertia-dominated impact force $\rho V_0^2 D_0^2$ in Fig. 3(a) for various impact speeds V_0, droplet diameters D_0, ridge morphologies n, and liquid viscosities μ. We use $\rho V_0^2 D_0^2$ as an independent variable along the x-axis because prior studies conducted with water droplets on flat substrates showed that $F_j/\rho V_0^2 D_0^2$ remains roughly constant [20] in the range of $30 < \mathrm{We} < 100$ overlapping with the range in this study. However, the adoption of $\rho V_0^2 D_0^2$ puzzles us since it represents the dynamic pressure ρV_0^2 multiplied by the projected droplet area D_0^2, or equivalently, the change of vertical momentum $\rho D_0^3 V_0/(D_0/V_0)$ in the impact event, neither of which captures the droplet retraction or the flow-focusing event. As such, our prior study found that $\rho V_0^2 D_0^2$ failed to capture F_j when variation in liquid viscosity comes into play [23], which rarely occurs if the process is completely inertia dominated, and a new scaling model for F_j was proposed to collapse all data points with varying viscosities. In addition to the previously explored viscous effects for flat superhydrophobic substrates, here, we highlight two new observations: (1) as presented in Fig. 3(b), the data for F_j for water droplets ($D_0 = 2.3$ mm) on the substrates with varying morphologies do not converge; (2) following the fact that the data for droplets with different viscosities on flat substrates do not converge, the values for F_j for the 75 wt%-glycerol droplets ($D_0 = 2.3$ mm) on the ridged substrates significantly deviate from all other data points. Therefore, in what follows, we aim to explain (i) the effect of the ridge morphology on F_j and (ii) the synergistic effect of the ridge morphology and liquid viscosity on F_j.

The magnitude of F_j is the largest on the flat substrate ($n = 1$), followed by a decrease in F_j with a decrease in n [Fig. 3(b)]. As inspired by prior studies [28,39], this trend could be related to a size-sensitive inertia-capillary time and speed dictated by the amount of liquid effectively participating in a flow-focusing event for a fixed n, scaled as $d_0 \sim n^{-1/3} D_0$ based on conservation of mass. Specifically, F_j is the total droplet mass $\sim \rho D_0^3$ multiplied by the inertia-capillary speed $\sqrt{\gamma_{LV}/\rho d_0}$ and divided by the inertia-capillary time $\sqrt{\rho d_0^3/\gamma_{LV}}$, resulting in $\gamma_{LV} D_0 n^{2/3}$. Although the effect of n is considered, this scaling fails to explain the largest value of F_j for the flat substrate ($n = 1$) and to reflect the effect of V_0. The flow-focusing time $t_{sj} = t_j - t_s$, the time interval spanning from the emergence of F_j to its peak, is plotted versus the inertia-dominated impact time D_0/V_0 in Fig. 3(c) and shows a decrease with an increase in n. This result may also suggest that a size-sensitive inertia-capillary time, which scales with the characteristic size d_0 of the liquid body effectively participating in the flow-focusing event, divided by the inertia-capillary speed $\sqrt{\gamma_{LV}/\rho d_0}$, is given by $n^{-1/2}\sqrt{\rho D_0^3/\gamma_{LV}}$. However, this timescale fails to reflect the effect of V_0 because Fig. 3(c)

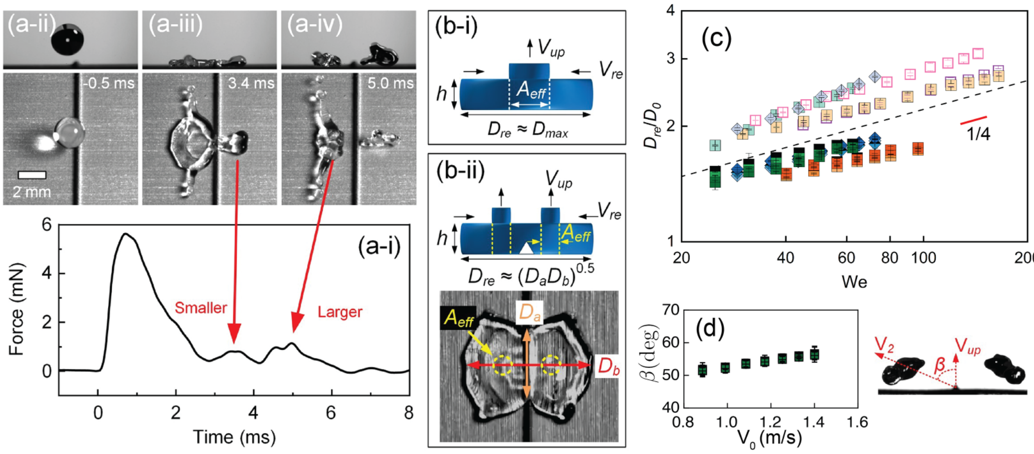

FIG. 4. (a–i) Temporal variation of the force exerted onto an "I"-shape ridged substrate by a droplet released at 70 mm, where the droplet base center is 0.55 mm away from the ridge. The images represent the droplet (ii) 0.5 ms before the impact, (iii) when the jump-off force provided by the smaller droplet reaches its peak, and (iv) when the jump-off force provided by the larger droplet reaches its peak. (b) Schematics of flow focusing and droplet geometric dimensions on (i) a flat and (ii) an "I"-shape ridged substrate. (c) Variation of the characteristic base diameter of the droplet normalized by the initial diameter D_{re}/D_0 with the Weber number. (d) Measured droplet jump-off angle β *versus* V_0, with the inset showing the definition of β.

suggests an increase in t_{sj} with a decrease in V_0. The above evidence suggests that droplet bouncing on the ridged substrates is driven by an intricate interaction between capillarity, inertia, and the droplet splitting event dictated by the ridge configuration represented by n.

C. The effects of ridge morphology on flow-focusing events

Before carrying out the analysis of the magnitude and timescale for F_j, it is essential to delineate what is directly inferred from the experimental data. Specifically, whether the measured value of F_j corresponds to a single force applied at the center of the main droplet or it represents a superposition of multiple synchronous forces ($F_j = nf_j$) acting at each flow-focusing area. The observations presented in Fig. 2 support the latter interpretation. As compared to the inertia-dominated first penetration, the second penetration occurs below each subdroplet, located away from the impact site [Fig. 1(c)]. As a test, a droplet with an offset distance of ∼0.55 mm between its center and the ridge was released at 70 mm to impact onto an "I"-shape ridged substrate. This offset distance leads to the emergence of two separated films with different volumes and hence with distinct dynamics. Figure 4(a) reveals two jump-off events associated with two jump-off forces; the earlier and smaller force corresponds to the smaller film, and the later and larger force represents the larger film. A combination of Figs. 1(c), 2, and 4(a) suggests that the single F_j observed in Fig. 2 represents a superposition of forces stemming from multiple synchronized flow-focusing events.

Figures 2(a-ii)–2(a-iv) suggest that the recoiling droplet imparting the force F_j on the substrate assumes a pancake-like shape with a characteristic base diameter D_{re}, a thickness h, and the retracting speed of V_{re}. This pancake-like droplet causes a small cylindrical domain(s) A_{eff} (the flow-focusing site) to be squeezed with a vertically redirected flow speed V_{up} determined from the mass conservation over the period of flow-focusing time. This horizontal-to-vertical redirection of flow is

$$D_{re}hV_{re} \sim nA_{\text{eff}}V_{up}, \tag{1}$$

as illustrated in Figs. 4(b-i) and 4(b-ii) on a flat and an "I"-shape ridged substrate, respectively, where n represents the number of synchronized flow-focusing events (sites). The pancake-like droplet thickness h scales with $\sqrt{\gamma_{LV} D_0/\rho V_0^2}$ by combining $D_{re}^2 h \sim D_0^3$ and a correlation $D_{re} \approx D_{\max} \sim D_0 \mathrm{We}^{1/4}$ [40], where $D_{\max}$ is the droplet maximal spreading diameter. On flat substrates, $D_{\max}$ equals D_{re}. On ridged substrates, the characteristic base diameter, which scales with the effective volume contributing to all flow-focusing events, is the geometric average $D_{re} = \sqrt{D_a D_b}$ of the liquid along the ridge D_a and that in between the adjacent ridges D_b measured right before D_a retreats [Fig. 4(b-ii)]. All values D_{re}/D_0 roughly follow the scaling of $\sim \mathrm{We}^{1/4}$ [Fig. 4(c)] [23]. The momentum redirection and the sudden emergence of F_j must be accompanied by a variation in the speed of the horizontally retracting film, which is chosen as the inertia-capillary speed $V_{re} \sim \sqrt{\gamma_{LV}/\rho D_0}$ for simplicity. Equation (1) yields the effective area of a flow-focusing site as $A_{\mathrm{eff}} \sim D_0^{5/4}\gamma_{LV}^{3/4}/(\rho^{3/4}V_0^{1/2}V_{up}n)$. The flow-focusing time, i.e., the duration of flow squeezing (horizontal-to-vertical redirection), is determined by the size of the flow-focusing site $\sqrt{A_{\mathrm{eff}}}$ dividing the speed V_{re} of the horizontally retracting film, which yields

$$t_{sj} \sim \frac{\sqrt{A_{\mathrm{eff}}}}{V_{re}} \sim \frac{D_0^{9/8}\rho^{1/8}}{n^{1/2}\gamma_{LV}^{1/8}V_0^{1/4}V_{up}^{1/2}}. \tag{2}$$

Now, Eq. (2) requires V_{up} in the flow-focusing process (within t_{sj}), whose measurement is impossible because such local dynamics at the droplet center is blocked by the oscillating interface. As a result, we assume that V_{up} scales with the droplet speed at its jump-off, which can be roughly estimated using energy conservation. Neglecting the kinetic energy of the oscillating interface, contact angle hysteresis [14,15], and the satellite microdroplets produced during droplet splitting, the energy balance before the droplet-substrate contact and after the jump-off of all subdroplets is given under the assumption that all droplets are spherical, by $mV_0^2/2 + \pi D_0^2\gamma_{LV} = mV_2^2/2 + n\pi d_0^2\gamma_{LV} + E_{\mathrm{vis}}$ [41,42], which further yields

$$V_2 = \sqrt{V_0^2 - 12(n^{1/3}-1)\gamma_{LV}/\rho D_0 - 12E_{\mathrm{vis}}/\pi D_0^3\rho} = V_{up}/\cos\beta, \tag{3}$$

where $m = \pi D_0^3\rho/6$ is the droplet mass and β is an experimentally defined angle between the vertical direction (V_{up}) and the direction of jump-off speed V_2 of the (sub-)droplets after jump-off [the inset in Fig. 4(d)]. We assume that on the flat surface, the entire pancake-like droplet with the volume $\sim D_0^3$ contributes to the viscous dissipation $E_{\mathrm{vis}} = E_{\mathrm{vis}}^{\mathrm{flat}}$ because the boundary layer thickness exceeds the droplet thickness $h \sim \sqrt{\gamma_{LV}D_0/\rho V_0^2}$. The viscous dissipation per unit volume and unit time is $\mu(\partial u/\partial z)^2 \sim \mu(V_0/h)^2$ [37], and we take the well-known droplet-substrate contact time (the inertia-capillary time [26]) $\sim\sqrt{\rho D_0^3/\gamma_{LV}}$ as the duration for viscous dissipation. We then obtain

$$E_{\mathrm{vis}}^{\mathrm{flat}} \sim c_{\mathrm{flat}}\mu V_0 D_0^2 \mathrm{We}^{3/2}, \tag{4}$$

where c_{flat} is a fitting coefficient to connect the scaling analysis of $E_{\mathrm{vis}}^{\mathrm{flat}}$ to the energy conservation.

Equation (3) indicates that V_2 slightly decreases with an increase in n and $V_2 = V_{up} \approx V_0$ for a water droplet impacting onto a flat substrate as $\beta = 0$ (vertical rebound) and $E_{\mathrm{vis}} \approx 0$. For water droplets impacting onto ridged substrates, $E_{\mathrm{vis}} \approx 0$. The measured value of β for water droplets on ridged substrates increases from $\sim 51^\circ$ to $\sim 57^\circ$ with an increase in V_0 and the effect of the ridge shape is weak [Fig. 4(d)]. Note here that treating β as a constant does not affect the results or verifications conducted in what follows, but we adopt the experimentally measured value for β. This is because the inertia-dominated lateral spreading speed scales with V_0 (some of the liquids keep spreading), while the retraction-induced vertical jump-off speed scales with V_{re}. As such, the scaling of $\tan\beta \sim V_0/\sqrt{\gamma_{LV}/\rho D_0}$ qualitatively suggests an increase of β with V_0.

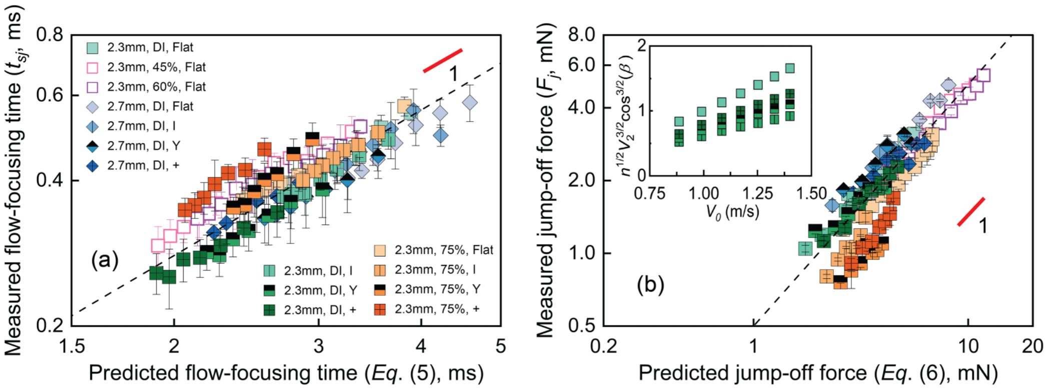

FIG. 5. (a) Variation of the measured flow-focusing time t_{sj} *versus* the value predicted using Eq. (5). (b) Variation of the measured jump-off force F_j *versus* the value predicted using Eq. (6), taking into account the viscous dissipation terms $E_{\text{vis}}^{\text{flat}}$. The inset shows the variation of the value $n^{-1/2}V_2^{-1/2}\cos^{-1/2}\beta$ with V_0 for water droplets with $D_0 = 2.3$ mm.

Substituting Eq. (3) into Eq. (2) yields the flow focusing time as

$$t_{sj} \sim \frac{D_0^{9/8}\rho^{1/8}}{n^{1/2}\gamma_{LV}^{1/8}V_0^{1/4}\left(V_0^2 - 12(n^{1/3}-1)\gamma_{LV}/\rho D_0 - 12E_{\text{vis}}/\pi D_0^3\rho\right)^{1/4}\cos^{1/2}\beta}. \tag{5}$$

The flow-focusing time t_{sj} measured experimentally is now presented versus its predicted value based on Eq. (5) with $c_{\text{flat}} = 0.01$ in $E_{\text{vis}}^{\text{flat}}$ [Fig. 5(a)], where most of the data points (except for those of 75 wt%-glycerol droplets on ridged substrates) collapse onto a straight line in contrast to Fig. 3(c). The values for t_{sj} for viscous droplets on the flat substrates reported in our prior investigation are included in Fig. 5(a) to support Eq. (5) [23]. The term $n^{-1/2}V_2^{-1/2}\cos^{-1/2}\beta$ in Eq. (5) (note that $V_2 = \sqrt{V_0^2 - 12(n^{1/3}-1)\gamma_{LV}/\rho D_0 - 12E_{\text{vis}}/\pi D_0^3\rho}$) reflects the effects of the ridge and suggests that a larger n corresponds to a smaller t_{sj}, in agreement with the trend shown in Fig. 3(c). Moreover, the trend that t_{sj} decreases with an increase in V_0 is revealed by Eq. (5).

With the knowledge of t_{sj}, the jump-off force F_j can then be estimated as the product of the droplet's total mass ρD_0^3 and the acceleration from 0 to V_{up} over the time interval t_{sj} to yield

$$F_j \sim n^{1/2}\cos^{3/2}\beta\,\rho^{7/8}D_0^{15/8}\gamma_{LV}^{1/8}V_0^{1/4}\left(V_0^2 - 12\left(n^{1/3}-1\right)\gamma_{LV}/\rho D_0 - 12E_{\text{vis}}/\pi D_0^3\rho\right)^{3/4}. \tag{6}$$

Equation (6) suggests that F_j increases with an increase in V_0, agreeing with the trend shown in Fig. 3(b). The term $n^{1/2}V_2^{3/2}\cos^{3/2}\beta$ in Eq. (6), which reflects the effect of the presence of ridges, is the largest for $n = 1$, followed by values for $n = 4$, $n = 3$, and $n = 2$ [the inset in Fig. 5(b)], in agreement with the observations in Fig. 3(b). This is because the term $n^{1/2}V_2^{3/2}$ increases with an increase in n, while the value of $\cos^{3/2}\beta$ for the flat substrate is much larger than those for the ridged substrates, namely 1 for $\beta = 0^\circ$ vs 0.4 for $\beta = 57^\circ$. Equation (6) reduces to $\rho^{7/8}D_0^{15/8}\gamma_{LV}^{1/8}V_0^{7/4}$ for water droplets on flat substrates [23] with $n = 1$ and $E_{\text{vis}} \approx 0$, which is further approximated as $\rho D_0^2 V_0^2$ (a special case for the flat substrate with negligible viscous dissipation), agreeing with prior experimental results [20]. With $c_{\text{flat}} = 0.01$ in $E_{\text{vis}}^{\text{flat}}$, the measured values F_j are now presented *versus* their predicted values based on Eq. (6) [Fig. 5(b)], showing a collapse of most data points onto a straight line as compared with those in Fig. 3(a), except for the data of 75 wt%-glycerol droplets on the ridged substrates. In the following text, therefore, we aim to explain and resolve this deviation by considering the synergistic effects of viscous dissipation and ridge morphology.

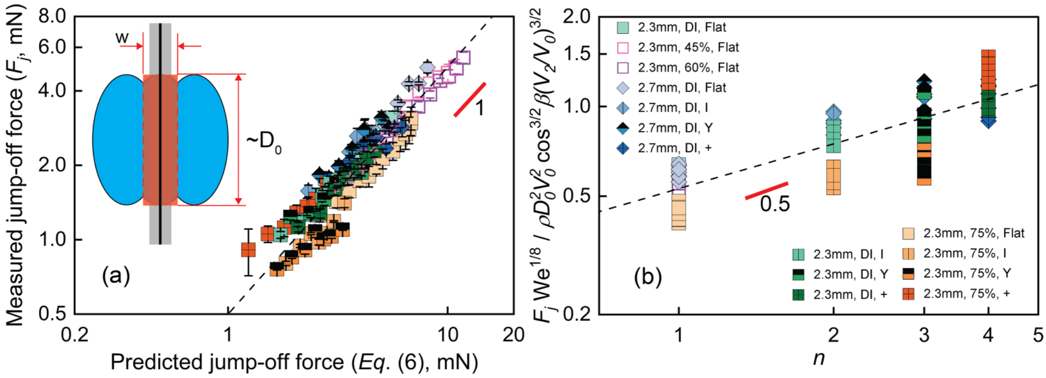

FIG. 6. (a) Variation of the measured jump-off force F_j *versus* the value predicted using Eq. (6) using $E_{\text{vis}}^{\text{flat}}$ and $E_{\text{vis}}^{\text{ridge}}$. The insert is the top-view sketch of a droplet spreading on the "I"-shape ridged substrate. The pink area is the volume subjected to viscous dissipation. (b) Variation of the value of $F_j \text{We}^{1/8}\rho^{-1}D_0^{-2}V_0^{-2}\cos^{-3/2}\beta(V_2/V_0)^{-3/2}$ with n.

D. Synergistic effects of viscous dissipation and ridge morphology on the droplet jump-off force

We envision that the deviation mentioned at the end of subsection C is caused by distinct viscous dissipation for droplets on flat and ridged substrates, where all liquids contribute to $E_{\text{vis}}^{\text{flat}}$ in the former case, whereas only the liquid body near the ridge contributes to $E_{\text{vis}}^{\text{ridge}}$ in the latter. Specifically, on flat substrates, all liquids must go through spreading and retraction before the flow focusing about the droplet center takes place. In comparison, on ridged substrates, the droplet jump-off and flow focusing are mainly driven by the earlier and faster retreating liquid from the ridge, rather than the rest of the liquid body (please refer to the discussion in Sec. III A). Therefore, the liquid volume affected by viscous dissipation is that of the liquid near the ridge [the pink area in the inset of Fig. 6(a)], given by $\sim D_0hwn/2$, where $w = 0.3$ mm is the ridge width. The division by 2 in $\sim D_0hwn/2$ originates from the fact that the "I"- ($n = 2$), "Y"- ($n = 3$), and "+"- ($n = 4$) shape ridges correspond to the numbers of 1, 1.5, and 2 ridges. Since the flow focusing takes place much earlier on the ridged substrates than on the flat substrates (Fig. 2), we adopt the impact time $\sim D_0/V_0$ instead of the inertia-capillary time $\sim\sqrt{\rho D_0^3/\gamma_{LV}}$ for the estimation of viscous dissipation, which yields

$$E_{\text{vis}}^{\text{ridge}} \sim c_{\text{ridge}} w \mu V_0 D_0 \text{We}^{1/2} n/2, \tag{7}$$

where $c_{\text{ridge}}w$ can be considered together as a fitting coefficient. Applying Eq. (4) with $c_{\text{flat}} = 0.01$ for flat substrates and Eq. (7) with $c_{\text{ridge}} = 7$ for ridged substrates, the measured F_j is now presented *versus* its predicted values based on Eq. (6) [Fig. 6(a)], collapsing all data points despite the variations in the impact speed V_0, droplet diameter D_0, ridge morphology n, and liquid viscosity μ.

To further verify Eq. (6) and especially the effects of ridge morphology n (the main objective of this study), we recast Eq. (6) by dividing it by $\rho D_0^2 V_0^2$ at both sides and further rearranging, which results in

$$\frac{F_j \text{We}^{1/8}}{\rho D_0^2 V_0^2 \cos^{3/2}\beta(V_2/V_0)^{3/2}} \sim n^{1/2}, \tag{8}$$

with $V_2/V_0 = \sqrt{1 - 12(n^{1/3} - 1)/\text{We} - 12E_{\text{vis}}/\pi D_0^3 \rho V_0^2}$. Then, the left-hand side of Eq. (8) that contains the measured value of F_j is plotted versus n in Fig. 6(b), collapsing all data points into a power law with a power of 0.5.

E. Discussion on the jump-off pressure

With the jump-off force explained, the pressure P_j imparted onto the substrate (an underlying mesh in Fig. 1) can be estimated as the jump-off force per flow-focusing site f_j divided by A_{eff}, as

$$P_j \sim \frac{n^{1/2}\cos^{5/2}\beta\rho^{13/8}D_0^{5/8}V_0^{3/4}\left(V_0^2 - 12\left(n^{1/3}-1\right)\gamma_{LV}/\rho D_0 - 12E_{\mathrm{vis}}/\pi D_0^3\rho\right)^{5/4}}{\gamma_{LV}^{5/8}}. \qquad (9)$$

Equation (9) indicates that P_j increases with an increase in V_0, which agrees with the experimental observation in Fig. 1(d), suggesting that a larger dynamic pressure $\rho V_0^2/2$ is required to penetrate a smaller pore. P_j is proportional to $n^{1/2}V_2^{5/2}$ and $\cos^{5/2}\beta$ in a competitive fashion, where the value of $n^{1/2}V_2^{5/2}$ for the case of $n = 2$ is at most 33% larger than in the case of $n = 1$, whereas the value of $\cos^{5/2}\beta$ with $\beta = 0^\circ$ ($n = 1$) is almost 5 times larger than in the case with $\beta = 57^\circ$ on the "I"-shape ridge ($n = 2$). This explains why a ridge placed between pores (does not block pores) suppresses liquid penetration (Fig. 1).

The predicted value of P_j given by Eq. (9) with a prefactor of 0.38 for both flat and "I"-shape ridged meshes is displayed in Fig. 1(d) as dashed lines, successfully capturing the measured values of the threshold dynamic pressure $\rho V_0^2/2$ that causes the second penetration. For flat meshes ($n = 1$), Eq. (9) reduces to $\sim\rho^{13/8}D_0^{5/8}V_0^{13/4}\gamma_{LV}^{-5/8}$, which is further approximated as $\sim\rho^{3/2}D_0^{1/2}V_0^3\gamma_{LV}^{-1/2}$ (a special case for flat substrates with negligible viscous dissipation), supported by the experimental results reported by Ryu *et al.* [6]. We remark that we have not attempted to measure the threshold droplet dynamic pressure for "Y"- or "+"-shape ridged meshes. The reason for that is that the effective area A_{eff} of the flow focusing is inversely proportional to n, and hence values of A_{eff} produced by "Y"- and "+"-shape ridges are too small to generate repeatable and credible experimental results. The viscous dissipation during liquid penetration through small pores also prevents us from measuring the threshold $\rho V_0^2/2$ for viscous droplets.

Further studies are encouraged to explore the jump-off force when substrate macro-pillars (e.g., pancake bouncing phenomena [43], where the droplet jump-off is caused by the upward motion of the liquids in between macro-pillars rather than the horizontal-to-vertical redirection of flow), substrate/structure flexibility [44–46], compound droplets [47], special surface structure design that causes irregular droplet behaviors (e.g., spinning [48]), and substrates with millimetric curvatures [39,49,50] are adopted.

IV. SUMMARY AND CONCLUSIONS

In summary, we have studied how the jump-off force and pressure imparted by a droplet to a superhydrophobic substrate are determined by the substrate macro-ridges by systematically varying the ridge morphology ("I"-shape, "Y"-shape, and "+"-shape ridges), droplet impact speed, droplet size, and liquid viscosity. For a flat superhydrophobic substrate, the droplet flow-focusing event caused by the uniformly receding droplet boundary occurs at only one site, leading to a single jump-off force and pressure imposed onto the substrate. In comparison, the presence of a ridge causes the liquid along the ridge to recede much faster than the rest, which breaks the symmetry and synchronicity of droplet retraction. We then provide two main arguments: (1) multiple flow-focusing events of split films take place synchronically and independently at different sites, and the measured jump-off force on ridged substrates is the superposition of multiple synchronic smaller forces; and (2) the viscosity dissipation originates from the entire droplet for a flat substrate and from the liquid near the ridge for ridged substrates. We then conducted an analysis to explain the measured droplet jump-off forces despite the variations in the substrate morphology, droplet impact speed, droplet size, and liquid viscosity. These arguments are also supported by the measured values of the flow-focusing time and the pressure imparted onto the meshes (accompanied by liquid penetration). We believe that the experimental results and the physical insights reported in this paper will benefit various technological applications, such as producing robust superhydrophobic surfaces, textiles for rainy conditions, and others.

ACKNOWLEDGMENTS

This work was partially supported by the National Natural Science Foundation of China (Grant No. 12202108), the Guangdong Basic and Applied Basic Research Foundation (Grants No. 2021A1515110184, No. 2022A1515011214, and No. 2021B0301030005), and the GTIIT-Technion Seed Grant.

The authors declare no competing financial interest.

DATA AVAILABILITY

The data that support the findings of this article are openly available [51].

[1] L. Bourouiba, The fluid dynamics of disease transmission, Annu. Rev. Fluid Mech. **53**, 473 (2021).

[2] C. J. Kähler and R. Hain, Fundamental protective mechanisms of face masks against droplet infections, J. Aerosol Sci. **148**, 105617 (2020).

[3] S. Sharma, R. Pinto, A. Saha, S. Chaudhuri, and S. Basu, On secondary atomization and blockage of surrogate cough droplets in single- and multilayer face masks, Sci. Adv. **7**, eabf0452 (2021).

[4] D. Soto, H.-L. Girard, A. Le Helloco, T. Binder, D. Quéré, and K. K. Varanasi, Droplet fragmentation using a mesh, Phys. Rev. Fluids **3**, 083602 (2018).

[5] Y. Zong, A. Oron, H. Liu, and Y. Jiang, Dynamic and quasi-static droplet penetration through meshes, Langmuir **39**, 9808 (2023).

[6] S. Ryu, P. Sen, Y. Nam, and C. Lee, Water penetration through a superhydrophobic mesh during a drop impact, Phys. Rev. Lett. **118**, 014501 (2017).

[7] A. Lafuma and D. Quéré, Superhydrophobic states, Nat. Mater. **2**, 457 (2003).

[8] A. B. D. Cassie and S. Baxter, Wettability of porous surfaces, Trans. Faraday Soc. **40**, 546 (1944).

[9] R. N. Wenzel, Resistance of solid surfaces to wetting by water, Ind. Eng. Chem. **28**, 988 (1936).

[10] Q. S. Zheng, Y. Yu, and Z. H. Zhao, Effects of hydraulic pressure on the stability and transition of wetting modes of superhydrophobic surfaces, Langmuir **21**, 12207 (2005).

[11] P. Papadopoulos, L. Mammen, X. Deng, D. Vollmer, and H.-J. Butt, How superhydrophobicity breaks down, Proc. Natl. Acad. Sci. USA **110**, 3254 (2013).

[12] M. Sbragaglia, A. M. Peters, C. Pirat, B. M. Borkent, R. G. H. Lammertink, M. Wessling, and D. Lohse, Spontaneous breakdown of superhydrophobicity, Phys. Rev. Lett. **99**, 156001 (2007).

[13] D. Quéré, Wetting and roughness, Annu. Rev. Mater. Sci. **38**, 71 (2008).

[14] Y. Jiang, Y. Sun, J. W. Drelich, and C.-H. Choi, Topography-dependent effective contact line in droplet depinning, Phys. Rev. Lett. **125**, 184502 (2020).

[15] Y. Jiang and C.-H. Choi, Droplet retention on superhydrophobic surfaces: A critical review, Adv. Mater. Interfaces **8**, 2001205 (2021).

[16] S. Qiao, S. Li, Q. Li, B. Li, K. Liu, and X.-Q. Feng, Friction of droplets sliding on microstructured superhydrophobic surfaces, Langmuir **33**, 13480 (2017).

[17] L. H. Kwong, R. Wilson, S. Kumar, Y. S. Crider, Y. Reyes Sanchez, D. Rempel, and A. Pillarisetti, Review of the breathability and filtration efficiency of common household materials for face masks, ACS Nano **15**, 5904 (2021).

[18] O. Aydin, B. Emon, S. Cheng, L. Hong, L. P. Chamorro, and M. T. A. Saif, Performance of fabrics for home-made masks against the spread of COVID-19 through droplets: A quantitative mechanistic study, Extreme Mech. Lett. **40**, 100924 (2020).

[19] X. Cheng, T.-P. Sun, and L. Gordillo, Drop impact dynamics: Impact force and stress distributions, Annu. Rev. Fluid Mech. **54**, 57 (2022).
[20] B. Zhang, V. Sanjay, S. Shi, Y. Zhao, C. Lv, X.-Q. Feng, and D. Lohse, Impact forces of water drops falling on superhydrophobic surfaces, Phys. Rev. Lett. **129**, 104501 (2022).
[21] D. Soto, A. B. De Larivière, X. Boutillon, C. Clanet, and D. Quéré, The force of impacting rain, Soft Matter **10**, 4929 (2014).
[22] T. Mouterde, T.-V. Nguyen, H. Takahashi, C. Clanet, I. Shimoyama, and D. Quéré, How merging droplets jump off a superhydrophobic surface: Measurements and model, Phys. Rev. Fluids **2**, 112001(R) (2017).
[23] J. Li, A. Oron, and Y. Jiang, Droplet jump-off force on a superhydrophobic surface, Phys. Rev. Fluids **8**, 113601 (2023).
[24] Z. Hu, F. Chu, and X. Wu, Double-peak characteristic of droplet impact force on superhydrophobic surfaces, Extreme Mech. Lett. **52**, 101665 (2022).
[25] C. Lee, Y. Nam, H. Lastakowski, J. I. Hur, S. Shin, A.-L. Biance, C. Pirat, C.-J. "CJ" Kim, and C. Ybert, Two types of Cassie-to-Wenzel wetting transitions on superhydrophobic surfaces during drop impact, Soft Matter **11**, 4592 (2015).
[26] D. Richard, C. Clanet, and D. Quéré, Contact time of a bouncing drop, Nature (London) **417**, 811 (2002).
[27] J. C. Bird, R. Dhiman, H.-M. Kwon, and K. K. Varanasi, Reducing the contact time of a bouncing drop, Nature (London) **503**, 385 (2013).
[28] A. Gauthier, S. Symon, C. Clanet, and D. Quéré, Water impacting on superhydrophobic macrotextures, Nat. Commun. **6**, 8001 (2015).
[29] See Supplemental Material at http://link.aps.org/supplemental/10.1103/cz2d-3vsd for the videos of droplet penetration through meshes and the variation of the impact forces together with the droplet dynamics.
[30] D. Bartolo, C. Josserand, and D. Bonn, Singular jets and bubbles in drop impact, Phys. Rev. Lett. **96**, 124501 (2006).
[31] S. Lin, D. Wang, L. Zhang, Y. Jin, Z. Li, E. Bonaccurso, Z. You, X. Deng, and L. Chen, Macrodrop-impact-mediated fluid microdispensing, Adv. Sci. **8**, 2101331 (2021).
[32] A. L. Yarin, Drop impact dynamics: Splashing, spreading, receding, bouncing …, Annu. Rev. Fluid Mech. **38**, 159 (2005).
[33] M. Bussmann, S. Chandra, and J. Mostaghimi, Modeling the splash of a droplet impacting a solid surface, Phys. Fluids **12**, 3121 (2000).
[34] C. Josserand and S. T. Thoroddsen, Drop impact on a solid surface, Annu. Rev. Fluid Mech. **48**, 365 (2016).
[35] J. Madejski, Solidification of droplets on a cold surface, Int. J. Heat Mass Transf. **19**, 1009 (1976).
[36] M. Pasandideh-Fard, Y. M. Qiao, S. Chandra, and J. Mostaghimi, Capillary effects during droplet impact on a solid surface, Phys. Fluids **8**, 650 (1996).
[37] S. Chandra and C. T. Avedisian, On the collision of a droplet with a solid surface, Proc. R. Soc. Lond. A **432**, 13 (1991).
[38] N. Laan, K. G. de Bruin, D. Bartolo, C. Josserand, and D. Bonn, Maximum diameter of impacting liquid droplets, Phys. Rev. Appl. **2**, 044018 (2014).
[39] P. Chantelot, A. Mazloomi Moqaddam, A. Gauthier, S. S. Chikatamarla, C. Clanet, I. V. Karlin, and D. Quéré, Water ring-bouncing on repellent singularities, Soft Matter **14**, 2227 (2018).
[40] C. Clanet, C. Béguin, D. Richard, and D. Quéré, Maximal deformation of an impacting drop, J. Fluid Mech. **517**, 199 (2004).
[41] A. Jha, P. Chantelot, C. Clanet, and D. Quéré, Viscous bouncing, Soft Matter **16**, 7270 (2020).
[42] M. Abolghasemibizaki, N. Dilmaghani, R. Mohammadi, and C. E. Castano, Viscous droplet impact on nonwettable textured surfaces, Langmuir **35**, 10752 (2019).
[43] Y. Liu, L. Moevius, X. Xu, T. Qian, J. M. Yeomans, and Z. Wang, Pancake bouncing on superhydrophobic surfaces, Nat. Phys. **10**, 515 (2014).
[44] T. Vasileiou, J. Gerber, J. Prautzsch, T. M. Schutzius, and D. Poulikakos, Superhydrophobicity enhancement through substrate flexibility, Proc. Natl Acad. Sci. USA **113**, 13307 (2016).

[45] Y. Jiang, Z. Xu, B. Li, J. Li, and D. Guan, Soft wetting: Droplet receding contact angles on soft superhydrophobic surfaces, Langmuir **39**, 15401 (2023).

[46] Y. Jiang and Z. Wang, Soft wetting: An analytical model for pillar topography- and softness-dependent droplet depinning force, Soft Matter **20**, 3593 (2024).

[47] N. Blanken, M. S. Saleem, M.-J. Thoraval, and C. Antonini, Impact of compound drops: A perspective, Curr. Opin. Colloid Interface Sci. **51**, 101389 (2021).

[48] H. Li, W. Fang, Y. Li, Q. Yang, M. Li, Q. Li, X.-Q. Feng, and Y. Song, Spontaneous droplets gyrating via asymmetric self-splitting on heterogeneous surfaces, Nat. Commun. **10**, 950 (2019).

[49] X. Gu, L. Chen, F. Wang, Y. Wang, Y. Li, W. Wu, M. Hu, and D. Deng, Numerical simulation of droplet impacting on a microstructured surface: Geometry, wettability, and control of jump-off force, Phys. Fluids **36**, 022025 (2024).

[50] Y. Liu, M. Andrew, J. Li, J. M. Yeomans, and Z. Wang, Symmetry breaking in drop bouncing on curved surfaces, Nat. Commun. **6**, 10034 (2015).

[51] J. Li, B. Li, Y. Jiang, Open data for “Droplet bouncing and jump-off forces on ridged substrates” figshare, Dataset (2025), https://doi.org/10.6084/m9.figshare.30067789.v4.